Processing and Application of Ceramics 12 [1] (2018) 27–35
https://doi.org/10.2298/PAC1801027Z

Effect of graphene orientation on microstructure and mechanical properties of silicon nitride ceramics

Yubing Zhang[1,2], Guangchun Xiao[1,2], Mingdong Yi[1,2], Chonghai Xu[1,2,3,*]

[1]*School of Mechanical and Automotive Engineering, Qilu University of Technology, Jinan, China*
[2]*Key Laboratory of Advanced Manufacturing and Measurement and Control Technology for Light Industry in Universities of Shandong, Qilu University of Technology, Jinan, China*
[3]*School of Mechanical Engineering, Shandong University, Jinan, China*

Received 24 August 2017; Received in revised form 11 November 2017; Accepted 31 January 2018

Abstract

Mechanical properties and microstructure of graphene platelets reinforced Si_3N_4 composites have been investigated and compared to monolithic Si_3N_4. The microstructure shows that graphene platelets are parallel to each other and perpendicular to the hot pressing direction. Fracture toughness and flexural strength of composite with 1 wt.% graphene measured on polished surface perpendicular to hot pressing direction are 8.7 MPa·m$^{1/2}$ and 892 MPa, respectively, which are increased about 14.5% and 20.2% compared with that parallel to hot pressing direction. The anisotropy of microstructure and mechanical properties of composites can be explained by the intrinsic anisotropy of graphene as well as the crack deflection energy release rate and the weak boundary bonding between graphene and Si_3N_4 caused by the thermal expansion mismatch.

Keywords: *graphene, anisotropy, silicon nitride ceramic, mechanical properties*

I. Introduction

During the last few years, graphene and the composites reinforced with graphene have been developed and a great number of articles have been published concerning the improved fracture toughness of those composites [1,2]. Ceramic materials, such as silicon nitride and alumina, have attracted tremendous attention due to their extreme hardness, superior wear resistance and good thermal stability. However, inherent brittleness limits their widespread application. The addition of graphene can improve the fracture toughness of ceramics, which could broaden the scope of application of ceramics. Chen *et al.* [3] prepared the graphene nanosheets reinforced alumina composites, which show about 43.5% increase in fracture toughness compared to the pure alumina sample. Dusza *et al.* [4] investigated the different types of graphene platelets as fillers in Si_3N_4 and found that fracture toughness was improved with the addition of graphene platelets. In addition, the composite containing the graphene platelets with the smallest dimension has the highest value of fracture toughness. The fracture toughness of Si_3N_4 can be improved with graphene as filler [5–7]. Moreover, the addition of graphene can enhance the tribological performance and electrical conductivity of Si_3N_4 based materials [8,9].

As it is well known, the composition and microstructure can greatly influence the mechanical properties of ceramic materials. The microstructure of ceramics depends on the processing method. Thus, in comparison to pressureless sintering, pressure sintering can result in higher density of ceramic materials. As for a two-dimensional sheet structure, however, graphene presents an orientation distribution paralleled with each other in ceramic composition under the pressure sintering [10,11]. It was found that the Young's modulus and shear modulus of Si_3N_4 based composite showed a noticeable anisotropy with the addition of graphene [12]. Rutkowski *et al.* [13] developed hot-pressed AlN/graphene composites and showed that graphene addition in larger amount resulted in higher anisotropy of heat flow in the composites. Celik *et al.* [14] prepared Al_2O_3/graphene composites by spark plasma sintering and found that anisotropic microstructure results in anisotropy of fracture toughness, elec-

* Corresponding author: tel/fax: +86 0531 8963 1131,
e-mail: *xch@qlu.edu.cn*

trical and thermal properties of composites. When the content of graphene is 3 vol.%, fracture toughness of the composite in the in-plane direction improves 26.7% compared to monolithic Al_2O_3, while reduces 17.2% in the through thickness direction [14].

In the present work, based on the microstructure characterization and mechanical properties testing, the influence of graphene orientation on mechanical properties of Si_3N_4/graphene composites was investigated. The aim of this present work was to investigate the influence in hot pressing direction and vertical to hot pressing direction. The various crack propagation directions and the energy release rate were showed and discussed.

II. Experimental

2.1. Materials and processing

The starting powders were commercially available Si_3N_4 powder (particle size ~0.5 μm, purity >99%, Nanjing Guanye Chemical Co, Ltd, China) and graphene platelets (GPLs) (thickness ~10 nm, diameter ~4 μm, purity >99.5%, Nanjing Xianfeng Nanomaterials Technology Co, Ltd, China). MgO (Sinopharm Chemical Reagent Co, Ltd, Shanghai, China), Al_2O_3 (Shanghai Chaowei Nanotechnology Co, Ltd, China) and Y_2O_3 (Shanghai Chaowei Nanotechnology Co, Ltd, China) were used as sintering aids with 2, 2 and 4 wt.%, respectively (i.e. 8 wt.% in total). Si_3N_4 as well as sintering aids were mixed in isopropyl alcohol by ultrasonic processing and mechanical agitation. The mixed slurry was subsequently milled for 56 h under nitrogen atmosphere. For preparing GPLs/Si_3N_4 composites, different amount of GPLs was dispersed in isopropyl alcohol by ultrasonic dispersion with surfactant polyvinylpyrrolidone as dispersant. The samples with 0, 0.5, 1, 1.5 and 2 wt.% of GPLs are denoted as SG_0–SG_2, where the subscripts indicate the content of GPLs. After that, the dispersed GPLs solution was added into the milled slurry (Si_3N_4 and sintering aids) and milled for another 8 h. After milling, the slurries were dried in vacuum at 100 °C for 24 h and then sieved. The dried mixed powders were sintered by hot pressing sintering at 1700 °C for 60 min under 25 MPa with both heating and cooling rate of 20 °C/min.

2.2. Characterization

The sintered samples with 42 mm in diameter and thickness of 5 mm were cut into bars. The bars were then ground and polished to obtain the dimensions of 3 × 4 × 30 mm and the average surface roughness less than 0.1 μm. The flexural strength was measured by the three-point bending test on a CMT5105 electromechanical universal testing machine (Shenzhen SANS Testing Machine Co., Ltd., China) with a span of 20 mm and a crosshead speed of 0.5 mm/min. The flexural strength of the samples was calculated by following equation:

$$\sigma_f = \frac{3 \cdot P \cdot L}{2 \cdot b \cdot h^2} \tag{1}$$

where σ_f is the flexural strength, P is the maximum loading force when the test bar was cracked, L is the span length, b is the width of the bar and h is the height of the test bar.

The hardness of the samples was determined using a Vickers Hardness Tester (HV-120, Huayin Corperation, China) at a load of 196 N and holding time of 15 s. The hardness of the samples was calculated by the following equation:

$$H_V = \frac{1.8544 \cdot P}{4 \cdot a^2} \tag{2}$$

where H_V is the hardness, P is the loading force, and a is the diagonal of the indentation.

Vickers indentation method was used to calculate the fracture toughness of samples with a Vickers Hardness Tester (HV-120, Huayin Corperation, China). The following equation was used to calculate the fracture toughness of the samples [15]:

$$K_{IC} = 0.203 \frac{H_V \cdot a^2}{c^{3/2}} \tag{3}$$

where K_{IC} is the fracture toughness, H_V is the hardness, a is the diagonal of the indentation, and c is the half-distance between the two crack tips. The measurement of hardness and fracture toughness was performed on the polished surfaces which were parallel to hot pressing direction (HPD) and vertical to hot pressing direction (VHPD), as shown in Fig. 1. Data for hardness, flexural strength and fracture toughness of composites were obtained on six samples.

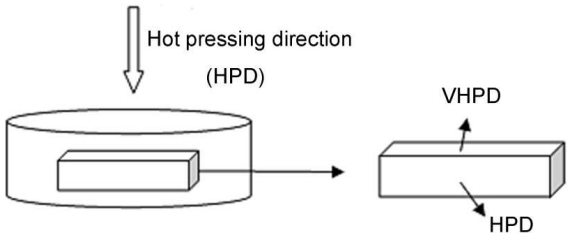

Figure 1. Scheme of hot pressing direction and the surfaces of HPD and VHPD

Microstructure characterization of samples was performed by a field emission scanning electron microscope (SEM) (SUPRATM 55, Germany). In order to observe the crack more clearly, the crack was introduced by diamond head first and then etched by 400 °C molten sodium hydroxide. X-ray diffraction (XRD, D8-ADVANCE, Bruker AXS, Germany) was used to check the phase composition. Raman spectroscopy (LabRAM HR800, Horibajy, France) was used for GPLs phase identification. Transmission electron microscope (TEM) and high resolution transmission electron microscope (HRTEM, JEM-2100, JEOL, Japan) were performed to observe the microstructure of the composite and the boundary surfaces of graphene and matrix. Archimedes method was used to measure the

density of the sintered materials. The theoretical density was calculated assuming a rule of mixtures and taking the density of 3.23 g/cm^3 for Si_3N_4 and 2.2 g/cm^3 for GPLs [16].

III. Results

3.1. Phase analysis

Figure 2 shows the XRD pattern of the sample SG_2 after sintering. It can be seen that only the peak of β-Si_3N_4 is present in the XRD pattern and the transformation from α-Si_3N_4 to β-Si_3N_4 is complete. In the case of the phase transformation, Rutkowski *et al.* [17] found that increase of graphene content resulted in incomplete transformation from α-Si_3N_4 to β-$Si_3N_4$and the reason relates to the oxide liquid phase. Due to the covalent nature of bonding and a low diffusivity of the constituents of the ceramics, Si_3N_4 is difficult to densify without sintering aids at relatively low sintering temperature. In this research, 2 wt.% of MgO, 2 wt.% of Al_2O_3 and 4 wt.% of Y_2O_3 were used as sintering aids. The sintering aids react with the surfaces of the Si_3N_4 to form a liquid phase which contributes to the transformation and the densification of composites [18]. In addition, adequate liquid phase is favourable for the rearrangement of GPLs and promotes the directional distribution of GPLs under the hot pressing sintering. As for the peak of GPLs, it was not found in Fig. 2. It may be related to the low content of graphene.

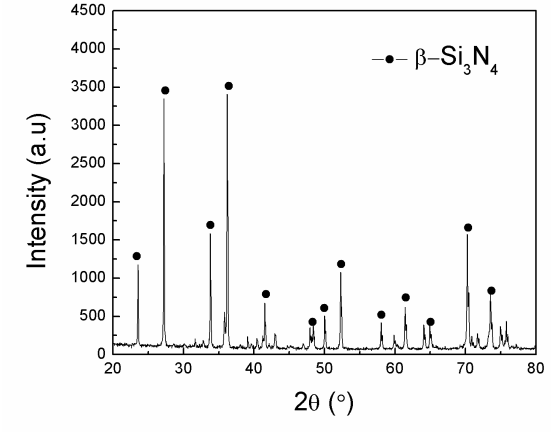

Figure 2. XRD pattern of the sintered SG_2 sample

Raman spectroscopy was used to identify GPLs in the composite. Figures 3a and 3b show the Raman spectra of the raw GPLs and the sintered SG_2 composite, respectively. The presence of bands D (1351 cm^{-1}), G (1588 cm^{-1}) and 2D (2700 cm^{-1}) can be seen, which are the representative peaks of GPLs [19,20]. XRD shows that new phase was not formed and Raman spectra confirm that GPLs remain in the matrix after sintering process. Thus, it can be concluded that there is no reaction between the matrix and GPLs.

Figure 4a shows TEM image of the raw GPLs, showing that the GPLs with a stacked structure have a large thickness. Figure 4b shows TEM images of the dispersed GPLs. It can be found that the thickness of the GPLs decreased after dispersing process.

3.2. Mechanical properties

Mechanical properties and relative density of the GPLs/Si_3N_4 composites are displayed in Table 1. The pure Si_3N_4 sample has the highest relative density of 99.2%. With the addition of GPLs up to 2 wt.%, relative density decreases slightly from 99.2% to 98%. It is very likely that the agglomeration of GPLs is the main reason. The GPLs addition in higher amount resulted in lower hardness of the composites measured on two polished surfaces (HPD and VHPD). It is possible that the GPLs as a softer reinforcement and a weak boundary between GPLs and Si_3N_4 decrease the hardness of composites. However, the hardness of the composites measured in VHPD is greater than that in HPD. The essential reason is not clear. It is probably related to the orientation distribution of GPLs. In the case of fracture toughness, it can be found that the fracture toughness of the composites measured on two polished surfaces increased with the increase of the content of GPLs and the maximum value was reached when the content of graphene is 1 wt.%. For example, the fracture tough-

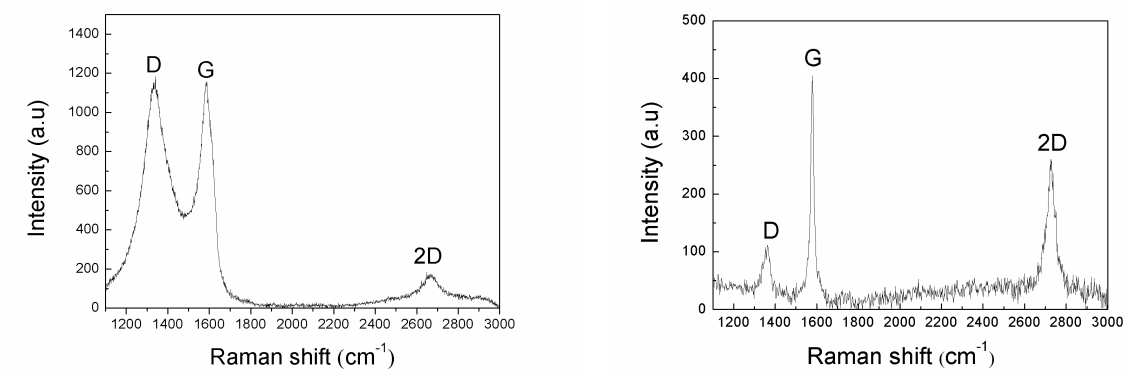

Figure 3. Raman spectra of: a) raw GPLs and b) sintered SG_2 sample

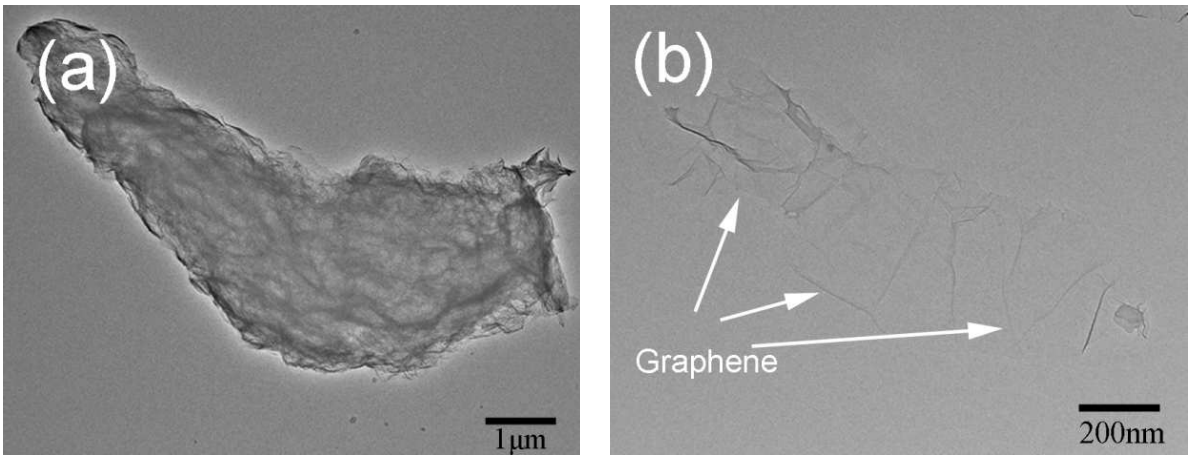

(a) (b)

Figure 4. TEM images of: a) raw GPLs and b) dispersed GPLs

nesses of the SG_1 composite measured in VHPD and HPD are 8.7 MPa·m$^{1/2}$ and 7.6 MPa·m$^{1/2}$, respectively, which is increase of about 38% and 21% as compared to the SG_0 ceramic. However, the addition of GPLs above this amount resulted in lower fracture toughness of the composites measured on two polished surfaces. A similar tendency has been found for the flexural strength of composites. With the addition of 1 wt.% GPLs, the flexural strength of the composite is 892 MPa (measured in VHPD) and 742 MPa (HPD), which is increase of about 36% and 13% as compared to the SG_0 ceramic, respectively. As shown in Table 1, both fracture toughness and flexural strength of the composites measured in VHPD are higher than that in HPD, i.e. they are increased by about 14.5% and 20.2%, respectively.

3.3. Microstructure

The microstructure of the sintered SG_1 sample is shown in Fig. 5 where the big white arrow in the top-right corner indicates hot pressing direction. From Fig. 5a it can be seen that GPLs are parallel to each other and perpendicular to the hot pressing direction. The orientation distribution of GPLs leads to the anisotropy of mechanical properties of the composites, which is in good agreement with mechanical characterization (Table 1). In addition, GPLs is homogeneously distributed in the matrix. However, GPLs with thickness exceeding 500 nm could be found, as shown in Fig. 5d, which is caused by the aggregation of GPLs. The weak boundary between GPLs and matrix leads to the pull-out of GPLs as shown in Figs. 5b and 5c. The pit left after the pull-out of GPLs can be seen in Fig. 5b. In contrast, the GPLs inserted in the matrix and stretched out from the fracture surface can be seen in Fig. 5c. Similar observation has been reported by Chen *et al.* [3] for alumina reinforced with graphene nanosheets composites. Due to the excellent mechanical properties of GPLs and the large contact area, the pull-out of GPLs must consume a vast energy which shortens the crack propagation distance compared to the ceramics without GPLs.

Figures 6a and 6b show the SEM images of the polished and etched surface of SG_1 ceramics in VHPD, respectively, whereas Figs. 6c and 6d display the SEM images in HPD. Due to the orientation distribution of GPLs, the GPLs can not be found in VHPD. From Fig. 6c it can be seen that GPLs exhibit a preferred orientation direction and that they are parallel to each other. Because of grinding and polishing process, there are some peeling off on the surface around GPLs (the weak boundary between matrix and GPLs).

Figures 7a and 7b show the SEM images of fracture surfaces and etched surface of SG_0 ceramics, and Figs. 7c and 7d display that of the SG_1 composite. It can be seen that the size of the Si_3N_4 grains in the SG_1 composite seems slightly smaller than that in the SG_0 composite. In addition, the sizes of Si_3N_4 grains of the SG_1 are more uniform than in the SG_0. Similar observation has been reported by Dusza *et al.* [4]. They found that the diameter of Si_3N_4 grain in composites reinforced with multilayer graphene nanosheets, exfoli-

Table 1. Mechanical properties and relative density of GPLs/Si_3N_4 composites

Specimen	Hardness [GPa]		Fracture toughness [MPa·m$^{1/2}$]		Flexural strength [MPa]		Relative density [%TD]
	VHPD	HPD	VHPD	HPD	VHPD	HPD	
SG_0	14.5 ± 0.3		6.3 ± 0.24		655 ± 12		99.2 ± 0.08
$SG_{0.5}$	14.3 ± 0.36	13.5 ± 0.31	7.9 ± 0.31	7.3 ± 0.21	832 ± 14	685 ± 15	99.1 ± 0.14
SG_1	13.9 ± 0.26	12.4 ± 0.34	8.7 ± 0.29	7.6 ± 0.31	892 ± 13	742 ± 19	98.9 ± 0.13
$SG_{1.5}$	13.3 ± 0.31	11.5 ± 0.26	8.2 ± 0.27	7.3 ± 0.16	813 ± 13	699 ± 17	98.6 ± 0.15
SG_2	13 ± 0.34	11.2 ± 0.28	7.5 ± 0.32	6.8 ± 0.28	760 ± 17	677 ± 21	98.0 ± 0.24

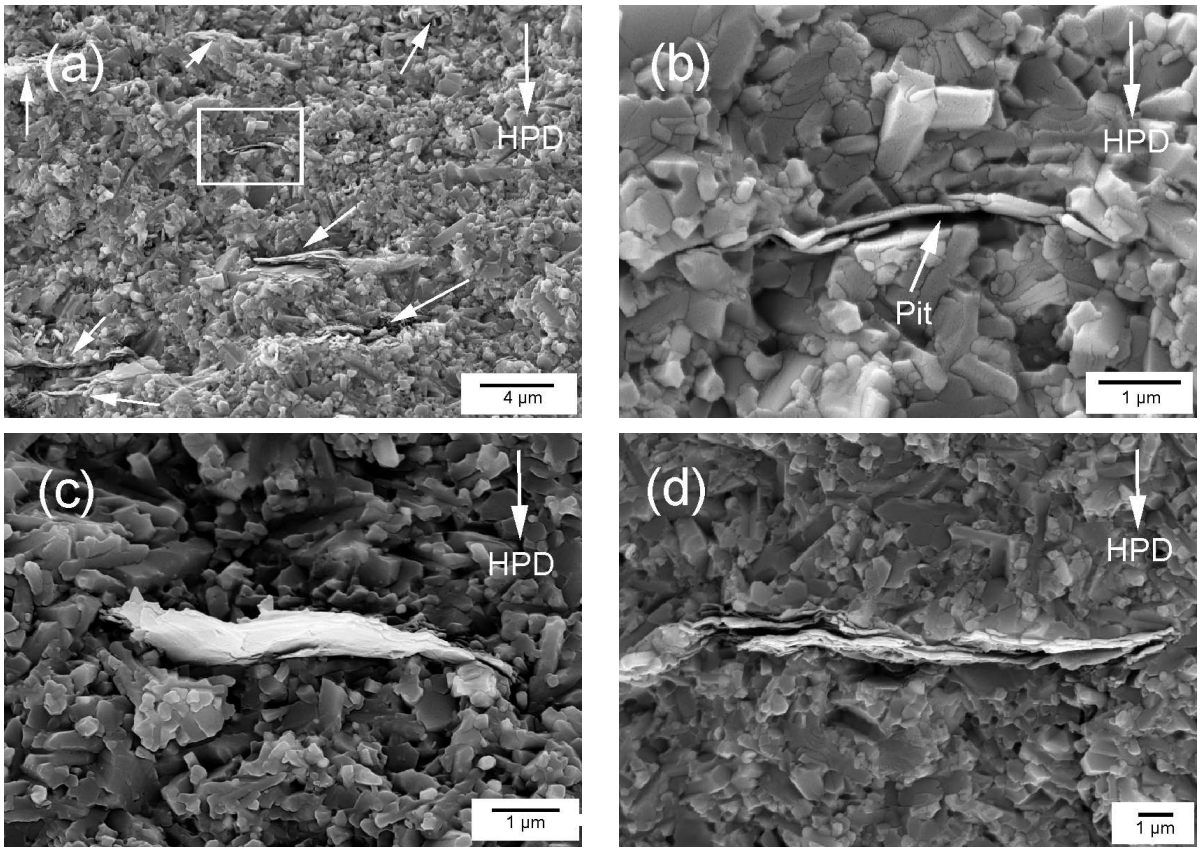

Figure 5. SEM images of SG1 sample: a) orientation distribution of graphene, b) the pit left after the pull-out of graphene, c) the pull-out of graphene, and d) the aggregation of graphene

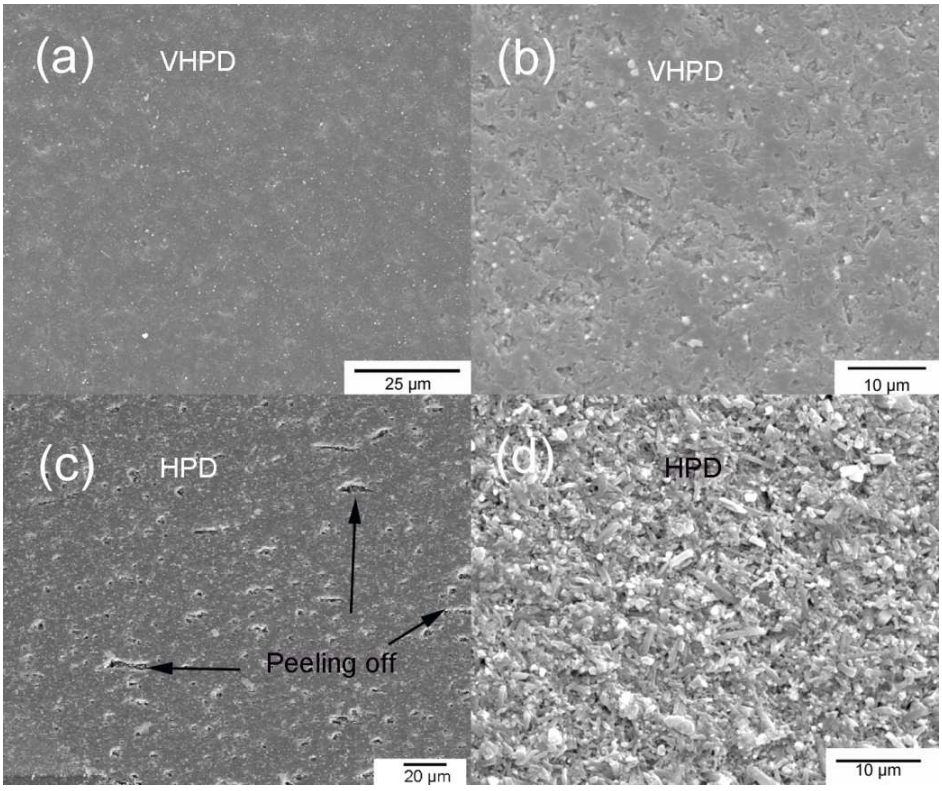

Figure 6. SEM images of SG_1 ceramics: a) polished surface in VHPD, b) etched surface in VHPD, c) polished surface in HPD and d) etched surface in HPD

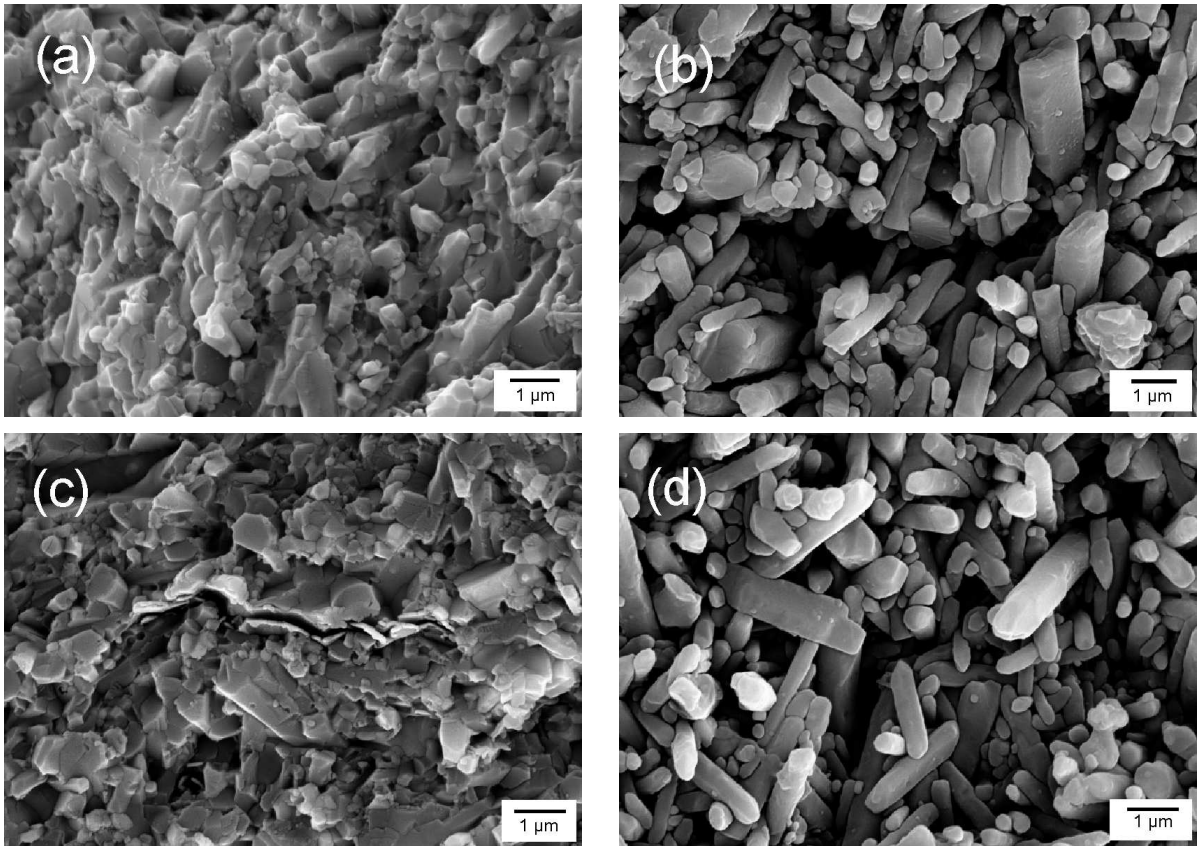

Figure 7. SEM images of the ceramics: the fracture surface (a) and etched surface (b) of monolithic Si_3N_4, the fracture surface (c) and etched surface (d) of SG_1 composite

ated graphite nanoplatelets and nano graphene platelets is on average very similar and is lower than that of the monolithic material [4]. According to our results the average Si_3N_4 grain diameter in the composites reinforced with GPLs is lower than that of the monolithic material. Finally, from Figs. 7a and 7c, it can be seen that the fracture mode in both materials is the mixed mode of transgranular and intergranular with intergranular being predominant.

Figure 8 shows TEM micrographs of the SG_1 composite. As shown in Fig. 8a, GPLs are located at the Si_3N_4/Si_3N_4 boundary, which effectively inhibits the matrix grain growth. As for the interfaces of Si_3N_4 grains and GPLs, it can be seen that there are two kinds of interfaces (Figs. 8a and 8b). One is no obvious intergranular phase as illustrated by the HRTEM in Fig. 8a and another one is the intergranular phase existing at the graphene/Si_3N_4 boundary as shown in Fig. 8b. Similar observation was reported by Dusza *et al.* [4] for silicon nitride reinforced with 1 wt.% graphene platelet composite. Furthermore, GPLs are located at the boundary and block matrix grain dissolution. GPLs inhibit the matrix grain growth and change the grain shape as shown in Fig. 8b. The grain growth of silicon nitride is in perpen-

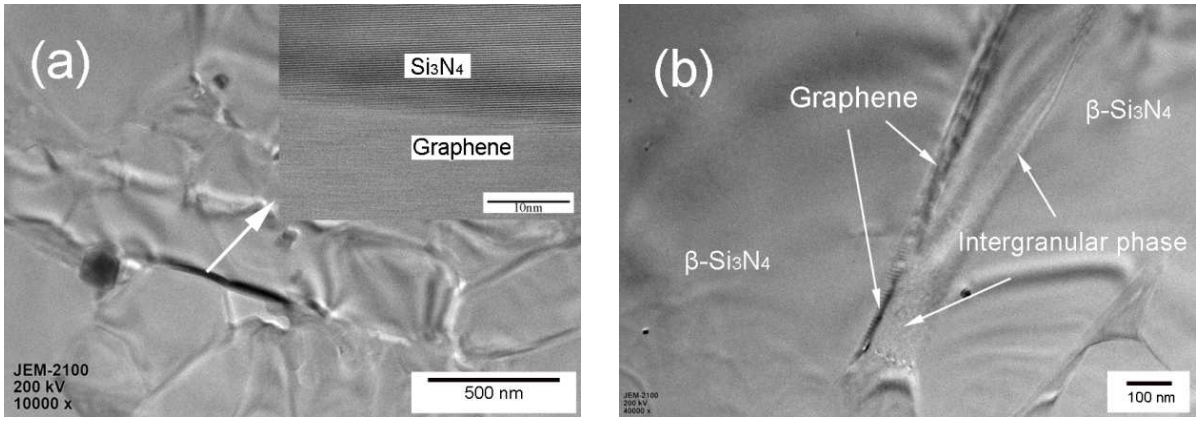

Figure 8. TEM images of the sintered SG_1 composite: a) graphene located at the boundary and HRTEM (inset) of the interface between of Si_3N_4 grains and graphene without intergranular phase, and b) intergranular phase at the graphene/Si_3N_4 boundary

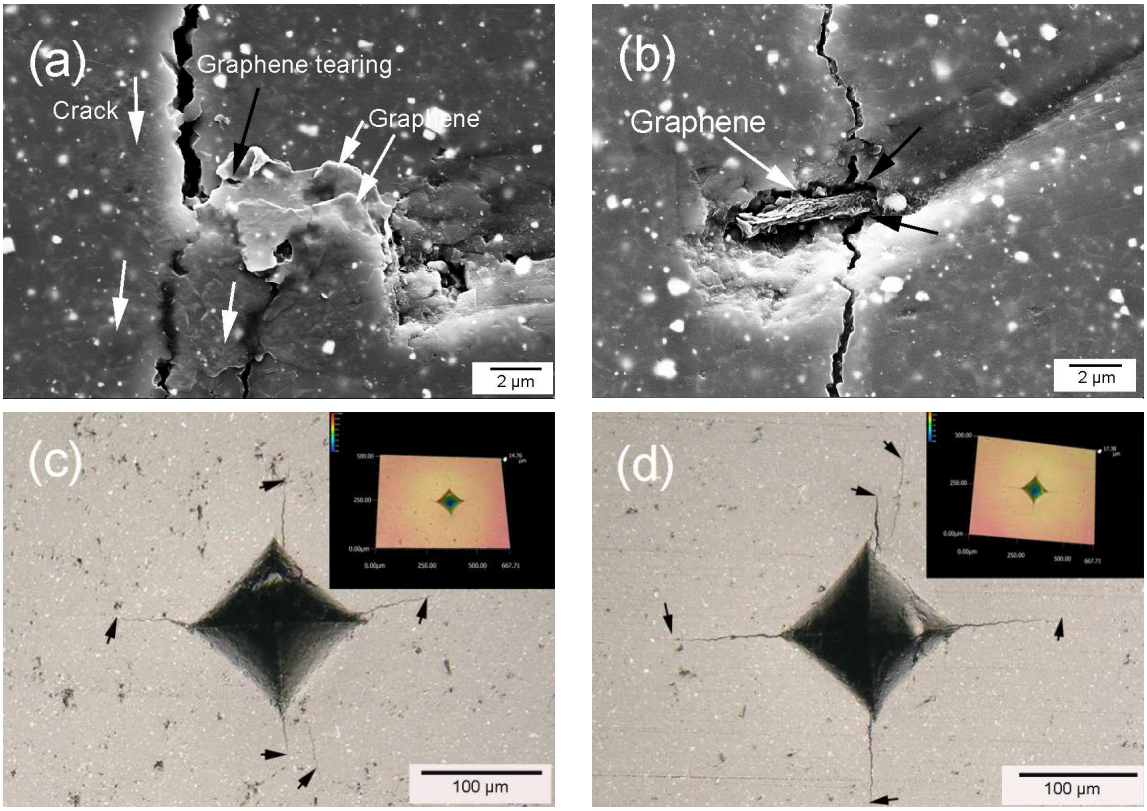

Figure 9. SEM images of SG_1 sample: a) crack branching in VHPD, b) graphene pull-out in HPD, c) crack propagation in VHPD, d) and crack propagation in HPD

dicular direction to the hot pressing axis. TEM images are in accordance with the analyses of Fig. 7.

When the indentation was performed in VHPD, crack branching, graphene pull-out and graphene tearing are main toughening mechanism, as shown in Figs. 9a and 9c. What is more, whatever the direction of crack propagation, the main toughening mechanism is similar. Therefore, the crack propagation in VHPD is isotropic and the crack length in different direction is similar as shown in Figs. 9a, 9c and 10a.

However, when the indentation was performed in HPD, the main toughening mechanism of GPLs was different. When the crack propagation direction is perpendicular to graphene, graphene pull-out and graphene break are predominant (Figs. 9b, 9d and 10b). Because of the high Young's modulus of graphene, graphene pull-out from matrix consumes a lot of energy. Figure 10b shows graphene break when the crack penetrates through GPLs and continues to extend. The energy consumed to penetrate through GPLs is expected to be very significant. When the crack propagation direction is parallel to graphene, due to the weak binding force between the layers of graphene, graphene delamination is the main toughening mechanism (Fig. 10d). Furthermore, because of the weak boundary between graphene and matrix, crack will extend and deflect along the obtuse angle direction between the crack propagation direction and graphene, as shown in Fig. 10c. Compared to graphene delamination and crack deflection, the toughening benefit of the graphene pull-out and the graphene break is greater. Because of this, the crack length perpendicular to HPD is much longer than that parallel to HPD, which can be seen in Fig. 9d. In addition, indentation depth in VHPD is 14.76 μm (Fig. 9c), which is shorter than that in HPD (17.38 μm (Fig. 9d). It indicates that the mechanical properties in VHPD are better than that in HPD.

Figure 11 depicts SEM image of the crack deflection when the crack propagation meets with GPLs in HPD. Crack deflection consumes a high amount of energy through a longer path during the crack propagation process.

IV. Discussion

It is no doubt that the orientation distribution of GPLs leads to the anisotropy of mechanical properties of composites. Relating to the effect of GPLs addition on the mechanical properties of composites, three factors have been considered.

The first is the intrinsic anisotropy of GPLs. As it is well known, GPLs are formed by the accumulation of monolayer graphene. The binding force of monolayer graphene with each other is very weak, while the Young's modulus of graphene along the graphene sheet is very high. It was found that the Young's modulus of a single crystal graphite along the graphite sheet is 1020 GPa against 36.5 GPa through the graphite sheet [21].

The second factor is the weak boundary between

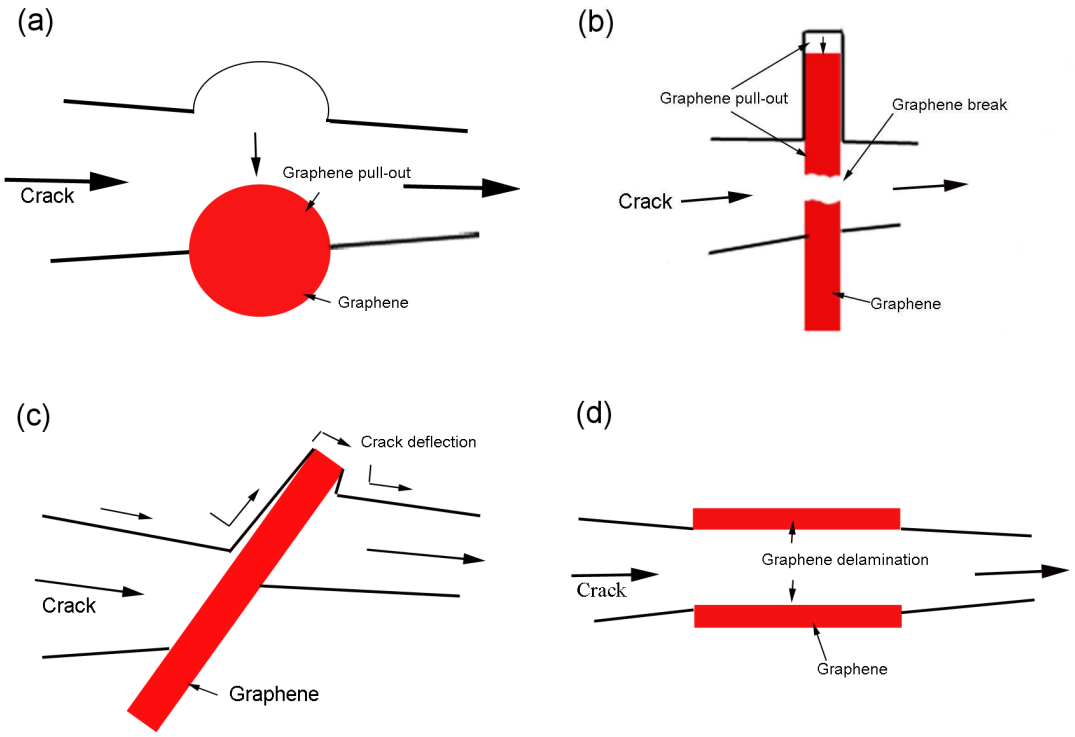

Figure 10. Schematics of: a) graphene pull-out in VHPD, b) graphene break in HPD, c) crack deflection in HPD and d) graphene delamination in HPD

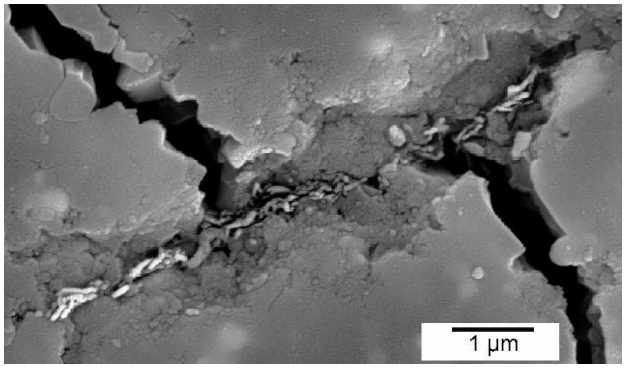

Figure 11. SEM image of the crack deflection

GPLs and matrix. This is caused by pores and defects, in the vicinity of the boundary and the residual stress caused by thermal expansion mismatch. The thermal expansion coefficient of Si_3N_4 (5×10^{-6} °C^{-1}) is lower than that of GPLs in the thickness direction and the thermal expansion coefficient of graphite (35×10^{-6} °C^{-1} in the thickness direction and 1×10^{-6} °C^{-1} for the in-plane) was considered as the same for graphene [22].

The last one is for the energy release rate of the oriented GPLs/Si_3N_4 composites. The analysis of the crack deflection energy release rate (ξ_d) was carried out by He et al. [23] and the corresponding expressions are as follows:

$$\xi_d = \left(k_1^2 + k_2^2\right)\left[\frac{1-\nu_1}{E_1} + \frac{1-\nu_2}{E_2}\right]\frac{1}{4\cdot\cosh^2\pi\varepsilon} \tag{4}$$

$$\varepsilon = \frac{1}{2\pi}\cdot\ln\left[\frac{1-\beta}{1+\beta}\right] \tag{5}$$

$$2\beta = \frac{\mu_1 + (1-2\nu_2) - \mu_2(1-2\nu_1)}{\mu_1(1-\nu_2) + \mu_2(1-\nu_1)} \tag{6}$$

where k is the stress intensity factor, ν is the Poisson's ratio, E is the elastic modulus, μ is the shear modulus. Also, the properties of the matrix and reinforcement are denoted as subscript number 1 and 2, respectively. The elastic modulus and Poisson's ratio of single crystal graphite (1020 GPa and 0.165 along graphite sheet and 36.5 GPa and 0.012 through graphite sheet) were used as that of graphene [21]. The elastic modulus and Poisson's ratio of Si_3N_4 are 324 GPa and 0.26, respectively [12]. In order to present the difference in the energy release rate of two directions, the ratio of ξ_d (HPD) to ξ_d (VHPD) was calculated and the value is 9.46. It means that the energy consumed in HPD is larger than that in VHPD in unit length. In other words, if one assumes that the energy distribution is uniform for four cracks caused by diamond head, it can be considered that the shorter the crack length is, the higher the energy release rate is.

V. Conclusions

The GPLs/Si_3N_4 composites with the anisotropic distribution of graphene were prepared by the hot pressing sintering. The analyses of XRD and Raman spectroscopy found that there was no reaction between matrix and GPLs. SEM observations presented that

graphene sheets were homogeneously distributed in the matrix and parallel with each other. They were located at the boundary and inhibited the matrix grain growth. The intrinsic anisotropy of graphene, the difference of the crack deflection energy release rate based on the anisotropic distribution of graphene and the weak boundary bonding between graphene and Si_3N_4 caused by the thermal expansion mismatch led to the anisotropy of mechanical properties.

Acknowledgement: This work was supported by the National Science Foundation of China (grant no. 51575285), Science and Technology Development Plan of Shandong Province (grant no. 2014GGX103001), Supported by the Key Research and Development Program of Shandong province (grant no. 2017GGX30136) and Research and Development Plan of Higher Education of Shandong Province (J14LB02).

References

1. Y.C. Fan, G. Igarashi, W. Jiang, L.J. Wang, A. Kawasaki, "Highly strain tolerant and tough ceramic composite by incorporation of grapheme", *Carbon*, **90** (2015) 274–283.
2. J. Liu, H. Yan, M.J. Reece, K. Jiang, "Toughening of zirconia/alumina composites by the addition of graphene platelets", *J. Eur. Ceram. Soc.*, **32** (2012) 4185–4193.
3. Y.F. Chen, J.Q. Bi, C.L. Yin, G.L. You, "Microstructure and fracture toughness of graphene nanosheets/alumina composites", *Ceram. Int.*, **40** (2014) 13883–13889.
4. J. Dusza, J. Morgiel, A. Duszová, L. Kvetková, M. Nosko, P. Kun, C. Balázsi, "Microstructure and fracture toughness of Si_3N_4 + graphene platelet composites", *J. Eur. Ceram. Soc.*, **32** (2012) 3389–3397.
5. L. Kvetková, A. Duszová, P. Hvizdoš, J. Dusza, P. Kunb, C. Balzási, "Fracture toughness and toughening mechanisms in graphene platelet reinforced Si_3N_4 composites", *Scripta. Mater.*, **66** (2012) 793–796.
6. L.S. Walker, V.R. Marotto, M.A. Rafiee, N. Koratkar, E.L. Corral, "Toughening in graphene geramic gomposites", *ACS Nano.*, **4** (2011) 3182–3190.
7. P. Kun, O. Tapasztó, F. Wéber, C. Balázsi, "Determination of structural and mechanical properties of multilayer graphene added silicon nitride-based composites", *Ceram. Int.*, **38** (2012) 211–216.
8. M. Belmonte, C. Ramirez, J. González-Julián, J. Schneider, P. Miranzo, M.I. Osendi, "The beneficial effect of graphene nanofillers on the tribological performance of ceramics", *Carbon*, **61** (2013) 431–435.
9. C. Ramirez, F.M. Figueiredo, P. Miranzo, P. Poza, M.I. Osendi, "Graphene nanoplatelet/silicon nitride composites with high electrical conductivity", *Carbon*, **50** (2012) 3607–3615.
10. O. Tapasztó, L. Tapasztó, H. Lemmel, V. Puchy, J. Dusza, C. Balázsi, K. Balázsi, "High orientation degree of graphene nanoplatelets in silicon nitride composites prepared by spark plasma sintering", *Ceram. Int.*, **42** (2016) 1002–1006.
11. Y. Zhang, G. Xiao, C. Xu, M. Yi, X. Meng, "Anisotropic fracture toughness and microstructure of graphene-reinforced TiC/Si_3N_4 composite", *J. Ceram. Sci. Tech.*, **7** (2016) 323–328.
12. H. Seiner, C. Ramirez, M. Koller, P. Sedlák, M. Landa, P. Miranzo, M. Belmonte, M.I. Osendi, "Elastic properties of silicon nitride ceramics reinforced with graphene nanofillers", *Mater. Design.*, **87** (2015) 675–680.
13. P. Rutkowski, D. Kata, K. Jankowski, W. Piekarczyk, "Thermal properties of hot-pressed aluminum nitride-graphene composites", *J. Therm. Anal. Calorim.*, **124** (2016) 93–100.
14. Y. Celik, A. Celik, E. Flahaut, E. Suvaci, "Anisotropic mechanical and functional properties of graphene-basedalumina matrix nanocomposites", *J. Eur. Ceram. Soc.*, **36** (2016) 2075–2086.
15. M. Fukuhara, K. Fukazawa, A. Fukawa, "Physical properties and cutting performance of silicon nitride ceramics", *Wear*, **102** [3] (1985) 195–210.
16. C. Ramirez, P. Miranzo, M. Belmonte, M.I. Osendi, P. Poza, S.M. Vega-Diaz, M. Terrones, "Extraordinary toughening enhancement and flexural strength in Si_3N_4 composites using graphene sheets", *J. Eur. Ceram. Soc.*, **34** (2014) 161–169.
17. P. Rutkowski, L. Stobierski, D. Zientara, L. Jaworska, P. Klimczyk, M. Urbanik, "The influence of the graphene additive on mechanical properties and wear of hot-pressed Si_3N_4 matrix composites", *J. Eur. Ceram. Soc.*, **35** (2015) 87–94.
18. M. Szafran, E. Bobryk, D. Kukla, A. Olszyna, "Si_3N_4-Al_2O_3-TiC-Y_2O_3 composites intended for the edges of cutting tools", *Ceram. Int.*, **26** (2000) 579–582.
19. C. Ramirez, M.I. Osendi, "Characterization of graphene nanoplatelets-Si_3N_4 composites by Raman spectroscopy", *J. Eur. Ceram. Soc.*, **33** (2013) 471–477.
20. A. Centeno, V.G. Rocha, B. Alonso, A. Fernández, C.F. Gutierrez-Gonzalez, R. Torrecillas, A. Zurutuza, "Graphene for tough and electroconductive alumina ceramics", *J. Eur. Ceram. Soc.*, **33** (2013) 3201–3210.
21. X.L. Meng, C.H. Xu, G.C. Xiao, M.D. Yi, Y.B. Zhang, "Microstructure and anisotropy of mechanical properties of graphene nanoplate toughened Al_2O_3-based ceramic composites", *Ceram. Int.*, **42** (2016) 16090–16095.
22. C. Ramirez, M.I. Osendi, "Toughening in ceramics containing graphene fillers", *Ceram. Int.*, **40** (2014) 11187–11192.
23. M.Y. He, J.W. Hutchinson, "Crack deflection at an interface between dissimilar elastic materials", *Int. J. Solids Struct.*, **25** (1989) 1053–1057.